Radial velocity confirmation of K2-100b: A young, highly irradiated, and low-density transiting hot Neptune

(article starts on next page)

Radial velocity confirmation of K2-100b: a young, highly irradiated, and low-density transiting hot Neptune

O. Barragán [1]★ S. Aigrain, [1] D. Kubyshkina, [2] D. Gandolfi, [3] J. Livingston, [4]
M. C. V. Fridlund, [5,6] L. Fossati, [2] J. Korth, [7] H. Parviainen, [8,9] L. Malavolta, [10]
E. Palle, [8,9] H. J. Deeg, [8,9] G. Nowak, [8,9] V. M. Rajpaul, [11] N. Zicher, [1] G. Antoniciello, [12]
N. Narita, [8,13,14,15] S. Albrecht, [16] L. R. Bedin, [17] J. Cabrera, [18] W. D. Cochran, [19]
J. de Leon, [4] Ph. Eigmüller, [18] A. Fukui, [20] V. Granata, [12] S. Grziwa, [7] E. Guenther, [21]
A. P. Hatzes, [21] N. Kusakabe, [13,15] D. W. Latham, [22] M. Libralato, [23] R. Luque [8,9]
P. Montañés-Rodríguez, [8,9] F. Murgas, [8,9] D. Nardiello, [12] I. Pagano, [10] G. Piotto, [12]
C. M. Persson, [5,6] S. Redfield [24] and M. Tamura [4,13,15]

Affiliations are listed at the end of the paper

ABSTRACT

We present a detailed analysis of HARPS-N radial velocity observations of K2-100, a young and active star in the Praesepe cluster, which hosts a transiting planet with a period of 1.7 d. We model the activity-induced radial velocity variations of the host star with a multidimensional Gaussian Process framework and detect a planetary signal of $10.6 \pm 3.0\,\mathrm{m\,s^{-1}}$, which matches the transit ephemeris, and translates to a planet mass of $21.8 \pm 6.2\,\mathrm{M_\oplus}$. We perform a suite of validation tests to confirm that our detected signal is genuine. This is the first mass measurement for a transiting planet in a young open cluster. The relatively low density of the planet, $2.04^{+0.66}_{-0.61}\,\mathrm{g\,cm^{-3}}$, implies that K2-100b retains a significant volatile envelope. We estimate that the planet is losing its atmosphere at a rate of 10^{11}–$10^{12}\,\mathrm{g\,s^{-1}}$ due to the high level of radiation it receives from its host star.

Key words: planets and satellites: individual: K2-100b – techniques: photometric – techniques: radial velocities.

1 INTRODUCTION

Theoretical evolution models predict that the most significant changes in the bulk and orbital parameters of exoplanets occur in the first few hundred Myr of their evolution (e.g. Adams & Laughlin 2006; Raymond et al. 2009; Kubyshkina et al. 2018a). Planets orbiting stars in young open clusters are thus particularly valuable tests of these models. The exquisite photometry collected by the *K2* space mission (Howell et al. 2014) and its observing strategy focused on the Ecliptic plane have enabled the detection of the first transiting planet candidates in star-forming regions and young stars (e.g. David et al. 2016a,b, 2019; Libralato et al. 2016; Mann et al. 2016a,b, 2017, 2018; Pepper et al. 2017; Livingston et al. 2018a, 2019), but none so far has mass measurements. Recent studies show that these young transiting exoplanets seem to be larger than their counterparts with similar periods orbiting more evolved stars (Mann

et al. 2016b). This suggests that photoevaporation by the host star plays an important role in shaping the planet atmosphere in the first few Gyr (as predicted by e.g. Owen & Wu 2013). However, expected evaporation rates depend strongly on planet mass, so measuring masses for these young transiting planets is important to test this scenario further.

This paper presents the first firm RV confirmation of a transiting planet in a young open cluster. K2-100 (EPIC 211990866, $\alpha_{\mathrm{J2000}} = 08{:}38{:}24.30$, $\delta_{\mathrm{J2000}} = +20{:}06{:}21.83$) is a bright ($V = 10.52$ mag) G-dwarf member (Kraus & Hillenbrand 2007) of the Praesepe cluster (NGC 2632, M44), which has an estimated age of 700–800 Myr and distance of 180 pc (Salaris et al. 2004; van Leeuwen 2009; Brandt & Huang 2015; Bossini et al. 2019). The transits of K2-100b, were discovered independently by Pope, Parviainen & Aigrain (2016) and Mann et al. (2017, hereafter M17) in *K2* campaign 5 data, though only the latter identified the host star as a Praesepe member. Analysis of the *K2* light curve alongside optical and infrared spectroscopy and adaptive optics imaging enabled M17 to rule out most false-positive scenarios and statistically validate

★ E-mail: oscar.barraganvillanueva@physics.ox.ac.uk

the planetary nature of K2-100b, alongside six other Praesepe candidates orbiting fainter stars. With a period of 1.67 d and 800 ppm transits, which implies a planet radius of 3.8 $R_\oplus$, K2-100b is a hot Neptune, and its bright host star made it a good candidate for further characterization.

The RV follow-up of planets in young open clusters is challenging because their host stars rotate rapidly and are magnetically active. This gives rise to quasi-periodic variations in the apparent stellar RV, which can be very difficult to disentangle from the planetary signal(s). Gaussian process regression (GPR) can be used to model activity signals in RV data (see e.g. Haywood et al. 2014; Grunblatt, Howard & Haywood 2015). This approach is even more powerful when complementary activity indicators extracted from the spectra are modelled alongside the RVs, as in the framework developed by Rajpaul et al. (2015, hereafter R15). In this paper, we used the framework of R15 to analyse RV observations of K2-100 and detect the reflex motion of the star induced by the transiting planet at the $>3\sigma$ level, despite the fact that the latter is of considerably lower amplitude than the activity-induced variations.

2 OBSERVATIONS

2.1 Photometry

K2 observed K2-100 as part of its Campaign 5 (C5, 2015-04-27 UTC to 2015-07-10 UTC) in long-cadence mode (30 min). This star was re-observed by *K2* in short cadence (1 min) mode on its Campaign 18 (C18, 2018-05-12 UTC to 2018-07-02 UTC). We downloaded the K2SFF (Vanderburg & Johnson 2014) light curve for C5 from the Mikulski Archive for Space Telescopes (https://arch ive.stsci.edu/k2/). We used the `lightkurve` package (Lightkurve Collaboration et al. 2018) to obtain the C18 *K2* light curve. We corrected for systematics using the pixel level decorrelation (PLD) as implemented in the `lightkurve` package.

Stefansson et al. (2018) performed a ground-based photometric follow-up of K2-100. They used the Engineered Diffuser instrument on the Astrophysical Research Council Telescope Imaging Camera (ARCTIC) imager located at the ARC 3.5 m Telescope at Apache Point Observatory. We downloaded the available public light curve from the online version of Stefansson et al. (2018) to use it in the analysis presented in Section 3.5.

We observed three transits of K2-100 with the MuSCAT2 multicolour photometer (Narita et al. 2019) installed in the Carlos Sanchez Telescope (TCS) in the Teide observatory on the nights of 2018-12-28 UTC, 2019-01-02 UTC, and 2019-01-22 UTC. All observations covered from 2 to 3.2 h around the expected mid-transit time, and were carried simultaneously in the r', i', and z' passbands with a common exposure time of 10 s. The photometry was done with the MuSCAT2 pipeline based on `PyTransit` (Parviainen 2015) and `LDTk` (Parviainen & Aigrain 2015).

We searched for transit timing variations (TTVs) using `PyTV` (Python Tool for Transit Variations, Korth, in preparation). We detected no TTVs; therefore, our results are consistent with a constant period model. This result, together with the precise ephemeris, implies that K2-100 can be efficiently scheduled for future follow-up observations.

2.2 Spectroscopy

We acquired 78 high-resolution ($R \approx 115\,000$) spectra of K2-100 with the HARPS-N spectrograph mounted at the 3.58-m Telescopio Nazionale Galileo at Roque de Los Muchachos observatory (La

Table 1. Stellar parameters.

Parameter	Value	Source
Stellar mass $M_\star$ ($M_\odot$)	1.15 ± 0.05	This work
Stellar radius $R_\star$ ($R_\odot$)	1.24 ± 0.05	This work
$v \sin i_\star$ (km s^{-1})	14 ± 2	This work
Stellar density $\rho_\star$ (g cm^{-3})	$0.85^{+0.12}_{-0.10}$	This work
Effective Temperature T_{eff} (K)	5945 ± 110	This work
Surface gravity $\log g_\star$ (cgs)	4.33 ± 0.10	This work
Iron abundance [Fe/H] (dex)	0.22 ± 0.09	This work
Star age (Myr)	750^{+4}_{-7}	B19
Spectral type	G0V	PM13

Note. B19 - Bossini et al. (2019), PM13 - Pecaut & Mamajek (2013).

Palma, Spain), as part of the observing programs CAT15B_35 (PI: Deeg), CAT15B_79 (PI: Palle), and ITP16_6 (PI: Malavolta). We processed the data using the dedicated HARPS-N pipeline and extracted the RVs by cross-correlating the HARPS-N spectra with a G2 numerical mask. We also extracted the Ca II activity indicator $\log R'_{HK}$ assuming a $B-V = 0.583$. Table A1 reports the HARPS-N RVs and their uncertainties along with the full width at half-maximum (FWHM) and the bisector inverse slope (BIS) of the cross-correlation function (CCF), $\log R_{HK}$, and the signal-to-noise (S/N) ratio per pixel at 5500 Å. For the analysis presented in Section 3.5, we removed 5 RV data points with a relative low S/N (<12).

3 DATA ANALYSIS

3.1 Stellar parameters

We determined the spectroscopic parameters of K2-100 from the co-added HARPS-N spectrum using the software Spectroscopy Made Easy (`SME, version 5.22`; Valenti & Piskunov 1996; Piskunov & Valenti 2017) along with ATLAS12 model atmospheres (Kurucz 2013) and atomic/molecular parameters from the VALD data base (Ryabchikova et al. 2015). The effective temperature T_{eff}, surface gravity $\log g_\star$, iron abundance [Fe/H], and projected rotational velocity $v \sin i_\star$ were measured following the same techniques described in, e.g. Fridlund et al. (2017), Gandolfi et al. (2017), and Persson et al. (2018). The micro- (v_{mic}) and macro-turbulent (v_{mac}) velocities were fixed through the empirical calibration equations of Bruntt et al. (2010) and Doyle et al. (2014). As a sanity check, we also carried out an independent spectroscopic analysis using the package `specmatch-emp` (Yee, Petigura & von Braun 2017). This code compares the observed spectrum with a library of 400 FGKM template spectra and minimizes the differences between the observed and the library data. The derived spectroscopic parameters agree within 1σ with those found by `SME`.

Following the method described in Gandolfi et al. (2008), we measured the interstellar extinction along the line of sight to the star and found that it is consistent with zero. We derived the stellar mass, radius, and age using the online interface `PARAM-1.3` (http://stev.oapd.inaf.it/cgi-bin/param) and `PARSEC` stellar tracks and isochrones (Bressan et al. 2012), along with the visual magnitude ($V = 10.56$; Mermilliod 1987), the GAIA parallax ($\pi = 5.2645 \pm 0.0678$ mas; Gaia Collaboration et al. 2018), and our effective temperature and iron abundance measurements. The derived stellar parameters are listed in Table 1. We note that the inferred supersolar metallicity of K2-100 ([Fe/H] = 0.22 ± 0.09) is consistent with previous values measured for Prae-
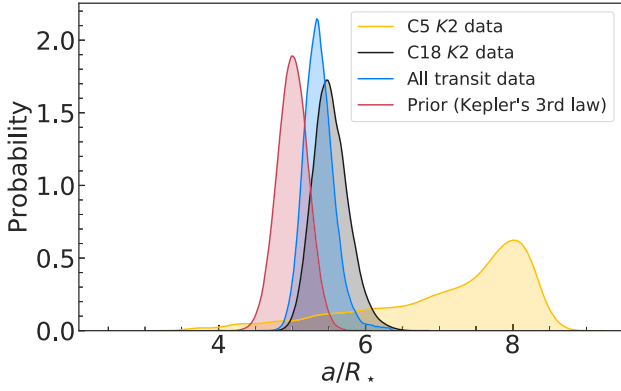
Figure 1. Posterior distribution for $a/R_\star$ for different analyses. The posterior distribution for $a/R_\star$ fitting only *K2* C5 data and *K2* C18 data are shown in yellow and black, respectively. Blue shows the posterior distribution for $a/R_\star$ fitting all available transits. We also show the prior on $a/R_\star$ using the derived stellar parameters in Section 3.1 and the planetary orbital period in red.

sepe stars (Pace, Pasquini & François 2008; Boesgaard, Roper & Lum 2013).

3.2 Stellar density analysis

M17 and Livingston et al. (2018b) noticed that K2-100's stellar density coming from the light curve analysis (assuming a circular orbit) differs from that from the spectroscopic parameters. This could be explained by a mischaracterized host star or an eccentric orbit. We discard the possibility that the star is mischaracterized given that our independent stellar parameter estimation is in agreement with the values reported by M17 and Livingston et al. (2018b). We also discard a significantly eccentric orbit given that the circularization time of K2-100's orbit (20 Myr, following Jackson, Greenberg & Barnes 2008) is significantly smaller than the system age.

We found out that this discrepancy was caused by a wide posterior distribution for $a/R_\star$ when analysing *K2* C5 data only. Fig. 1 shows the posterior distribution for the scaled semimajor axis, $a/R_\star$ (that relates directly with stellar density, see e.g. Winn 2010), by fitting C5 *K2* data only, C18 *K2* data only, and also by fitting all available transits. We set uniform priors on $a/R_\star$ for all cases. When fitting the C5 *K2* data, the MCMC converges to a solution which produces a wide posterior for $a/R_\star$ with median and 68 per cent credible interval given by $7.40^{+0.70}_{-1.75}$. This solution translates to a stellar density of $2.73^{+0.85}_{-1.62}$ g cm^{-3}. These values are similar to the values reported by M17 and Livingston et al. (2018b). When fitting all available transits, the MCMC sampling converges to a narrower posterior distribution with a inferred value of $a/R_\star = 5.36^{+0.25}_{-0.20}$ (we note that this value is still inside the posterior distribution found by fitting only C5 *K2* data). This value gives a stellar density of $\rho_\star = 1.04 \pm 0.15$ g cm^{-3}, which is consistent with the value derived in Section 3.1 (see Fig. 1). We note that when fitting the C18 *K2* alone we also get an $a/R_\star$ which is consistent with the expected value of $a/R_\star$ from Kepler's third law and the stellar parameters derived in Section 3.1. The new analysis including all available transits suggests that the planetary orbit is nearly circular, therefore we assume a circular orbit for K2-100b's in the rest of the manuscript. In order to speed-up convergence for the final analysis presented in Section 3.5, we used the derived stellar

parameters and Kepler's third law to set a Gaussian prior on $a/R_\star$ (see Fig. 1).

We note that the inferred $a/R_\star$ has a direct effect on the geometry on the system. For instance, the orbital inclination, planet radius, and other derived quantities differ from those reported in M17 and Livingston et al. (2018b).

3.3 Planet validation

K2-100b was first validated by Mann et al. (2017), who computed a false-positive probability (FPP) of 0.36 per cent using the `vespa` software package (Morton 2012). Livingston et al. (2018b) subsequently analysed the *K2* data (as processed by `k2phot`; Petigura et al. 2015) and obtained a slightly higher FPP of 1.2 per cent, just above their validation threshold of 1 per cent. This disagreement in FPP is comparatively small, and likely results from the use of different photometric pipelines, as well as stellar parameter estimates. We have used the new information contained in the short cadence *K2* C18 photometry of K2-100 and our simultaneous multiband MuSCAT2 photometry to revisit the FPP of K2-100b. The short cadence *K2* data put tighter constraints on the transit shape than was possible with the long cadence data from C5, which in turn has a significant impact on the FPP. We now obtain an extremely low FPP of $\lesssim 10^{-6}$ for K2-100b using `vespa`.

We can also independently constrain the possibility of various false-positive scenarios by measuring $r_p \equiv R_p/R_\star$ in different bandpasses (see e.g. Parviainen et al. 2019). We performed a fit to all our available flattened transits allowing for a free r_p for each band with uniform priors between [0,0.05]. We got $r_{p,K2} = 0.0286 \pm 0.0003$, $r_{p,\mathrm{ARCTIC}} = 0.0308 \pm 0.0011$, $r_{p,r} = 0.0241 \pm 0.0015$, $r_{p,i} = 0.0263 \pm 0.0015$, $r_{p,z} = 0.0281 \pm 0.0019$; the agreement of r_p in these bandpasses is inconsistent with most false-positive scenarios, thus confirming the `vespa` result.

3.4 RV analysis using multidimensional GP

In this work, we use the GP framework presented by R15 to model the RV data along with the $\log R'_{\mathrm{HK}}$ and BIS. Briefly, this approach assumes that all stellar activity signals can be modelled by the same latent variable $G(t)$ (and its derivatives) which is described by a zero-mean GP and a covariance function γ. Following R15, the RV, $\log R'_{\mathrm{HK}}$ and BIS time series can be modelled as

$$\Delta \mathrm{RV} = V_c G(t) + V_r \dot{G}(t),$$

$$\log R'_{\mathrm{HK}} = L_c G(t),$$

$$\mathrm{BIS} = B_c G(t) + B_r \dot{G}(t), \tag{1}$$

respectively. The variables V_c, V_r, L_c, B_c, and B_r are free parameters which relate the individual time series to an underlying Gaussian process $G(t)$. The GP itself is a latent (unobserved) variable, which can be loosely interpreted as representing the projected area of the visible stellar disc that is covered in spots or active regions at a given time. The GP is assumed to have zero mean and covariance matrix **K**, where $K_{ij} = \gamma(t_i, t_j)$. Following R15, we adopt the quasi-periodic covariance function

$$\gamma(t_i, t_j) = \exp\left[-\frac{\sin^2[\pi(t_i - t_j)/P_{\mathrm{GP}}]}{2\lambda_{\mathrm{P}}^2} - \frac{(t_i - t_j)^2}{2\lambda_{\mathrm{e}}^2} \right], \tag{2}$$

where P_{GP} is the period of the activity signal, λ_{P} the inverse of the harmonic complexity, and λ_{e} is the long-term evolution time-scale. This choice of covariance function is widely used to

model stellar activity signals in both photometry and RVs (see e.g. Aigrain, Pont & Zucker 2012; Haywood et al. 2014 and R15). The full expressions for the covariance between the three types of observations are given in R15.

3.5 RV and transit modelling

We used the open source code pyaneti (Barragán, Gandolfi & Antoniciello 2019) to model the light curve and RV data. We modified pyaneti's public version to allow for multiband transit and GP analyses. We also implemented the multidimensional GP approach described in Section 3.4 and R15. We used exotrending (Barragán & Gandolfi 2017) to isolate each transit and to remove long-term trends in the light curves as described in Barragán et al. (2018a,b). We resampled the model over 10 steps to account for the long-cadence (30 min, C5) *K2* data (Kipping 2010). We did not re-sample the model for *K2* and ground-based short-cadence data. We assumed that the difference of transit depth between different bands is negligible; therefore, we fit for a single radius ratio $R_p/R_\star$ for all the bands. We fitted for the limb-darkening parameters for each band using uniform priors and the parametrization described by Kipping (2013). We have assumed a circular orbit (see Section 3.2).

We performed a joint fit of all transits together with the RV, $\log R'_{HK}$, and BIS time series using the approach presented in Section 3.4. A summary of the fitted parameters and priors are presented in Table 2. We used 500 chains to sample the parameter space (38 free parameters). For the burning-in phase we used the last 5000 of converged chains with a thin factor of 10, leading to a final number of 250 000 independent points for each fitted parameter.

4 RESULTS AND DISCUSSION

Fig. 2 shows the RV, $\log R'_{HK}$ and BIS time series together with the inferred models. We also show the phase-folded RV and transit models, along with the data points in Figs 3 and 4, respectively. We inferred a planetary induced RV semi-amplitude of $10.6 \pm 3.0 \, \mathrm{m \, s^{-1}}$, which translates into a planet mass of $21.8 \pm 6.2 \, M_\oplus$. Other parameter estimates are presented in Table 2.

We note that we also analysed the RV data set with standard RV analysis techniques, such as Fourier decomposition (e.g. Pepe et al. 2013; Barragán et al. 2018a) and GPs trained with photometry (e.g. Barragán et al. 2018b; Malavolta et al. 2018). We found hints of the induced Doppler signal with a significance $\lesssim 2\sigma$. This shows that the simultaneous regression of the activity/asymmetry indicators play a fundamental role to measure the Doppler semi-amplitude with higher precision.

As a first check of the validity of our detection, we compare the Bayesian information criteria (BIC; see e.g. Burnham & Anderson 2002). We repeated the analysis presented in Section 3.5 by fitting a model with and without planet. We model only the RV-related time series, i.e. with no transit modelling. For the fit with planet, we set priors on the ephemeris coming from the transit analysis. We conclude that the model including the planet signal is strongly preferred over the model without it with a $\Delta BIC = 26$.

Rajpaul, Aigrain & Roberts (2016) showed that spurious RV detection of planets around active stars can arise due to a combination of complex activity models and the window function of the observations. To check that this is not the case here, we created 250 synthetic RV, $\log R'_{HK}$, and BIS time series using the best-fitting GP model, with no planet in the RV data set. We added white noise

to each point from a Gaussian distribution with standard deviation as the nominal error bar of each data point. We ran an MCMC fit as the one described in Section 3.5 (without transit data) for each data set, allowing for an RV signal with priors on the ephemeris of the planet. These simulations give rise to a 'detection' (we define a 'detection' as a signal with a significance $>2\sigma$) only in 0.4 per cent of the cases. We then repeat the experiment creating 250 more mock data sets, but this time injecting a coherent signal with an amplitude of $10 \, \mathrm{m \, s^{-1}}$ in the RV data set and same ephemeris as K2-100b. For this case, we have a 'detection' on 90 per cent of the runs. These results suggest that the planetary signal we detected in the real data is genuine.

As a further test of the reliability of our detection, we also extracted the RV measurements with a K5 numerical mask, and repeated the analysis presented in Section 3.5. We found an amplitude of $K = 12.4 \pm 3.5 \, \mathrm{m \, s^{-1}}$, which is within 1σ of the value obtained with the RVs extracted using the fiducial G2 mask.

Fig. 5 shows a planet density versus insolation plot for small planets ($R_p < 4 \, R_\oplus$) with masses measured to better than 50 per cent as listed in the TEPCAT catalogue (Southworth 2011; http://www.astro.keele.ac.uk/jkt/tepcat/). The plot also shows the limit of $650 \, F_\oplus$ given by Lundkvist et al. (2016) likely related to the presence/lack of a hydrogen-dominated atmosphere as a consequence of strong atmospheric escape. We find that for weakly irradiated planets ($< 650 \, F_\oplus$), low (sub-Earth) densities are common, in contrast to highly irradiated for which most of the planets have densities equal or larger than that of the Earth, with only two exceptions: NGTS-4b (West et al. 2019) and K2-100b. We discuss in more detail these two planets below.

Fig. 6 shows the position of K2-100b in a mass–radius diagram together with two-layer composition models by Zeng, Sasselov & Jacobsen (2016). With a mass of $21.8 \pm 6.2 \, M_\oplus$, a radius of $3.88 \pm 0.16 \, R_\oplus$, and a density of $2.04^{+0.66}_{-0.61} \, \mathrm{g \, cm^{-3}}$, we expect that K2-100b is a planet with a solid core with a significant volatile envelope. Fig. 6 also shows all highly irradiated small planets from Fig. 5. We find that all relatively low mass ($\lesssim 10 \, M_\oplus$) planets have densities higher than that of the Earth and they are consistent with a composition made of different mixtures of iron and silicates. This can be explained by the fact that close-in, low-mass planets beyond this insolation limit are expected to lose their primordial H/He atmospheres (e.g. Lundkvist et al. 2016). For planets with higher masses ($>10 \, M_\oplus$), instead, bulk densities are typically lower than that of the Earth and compositions range from mixes of silicates and water to solid cores with volatile envelopes. In fact, West et al. (2019) argue that NGTS-4b's relative low density may be caused by a relatively high core mass, which enables the planet to retain a significant volatile envelope.

Given the system's youth and short orbital separation, we model the past and future planetary atmospheric evolution, in particular to estimate if (and when) the planet will lose its envelope. To this end, we employed the planetary atmospheric evolution scheme described by Kubyshkina et al. (2018b, 2019, hereafter K18b and K19, respectively). This is based on a combination of model grids and analytical approximations. They comprise models providing atmospheric mass-loss rates as a function of system parameters (K18b), models enabling to estimate the atmospheric mass fraction as a function of planetary parameters (i.e. radius, mass, equilibrium temperature; Johnstone et al. 2015), and the Mesa/MIST grid of stellar evolutionary tracks to account for the evolution of the stellar bolometric luminosity (Choi et al. 2016). We model the past and future evolution of the stellar rotation period using a prescription similar to the empirical period–colour–age relation of Mamajek &

Table 2. K2-100b parameters.

Parameter	Prior[a]	Value[b]
Model parameters for K2-100b		
Orbital period P_{orb} (d)	$\mathcal{U}[1.6737, 1.6740]$	$1.673\,903\,5 \pm 0.000\,000\,4$
Transit epoch T_0 (BJD - 2450000)	$\mathcal{U}[7140.70, 7140.75]$	$7\,140.719\,41 \pm 0.000\,27$
e	$\mathcal{F}[0]$	0
$\omega_\star$	$\mathcal{F}[\pi/2]$	$\pi/2$
Scaled semimajor axis $a/R_\star$	$\mathcal{N}[5.01, 0.21]$	5.21 ± 0.13
Scaled planetary radius $R_p/R_\star$	$\mathcal{U}[0, 0.05]$	$0.028\,67 \pm 0.000\,28$
Impact parameter, b	$\mathcal{U}[0, 1]$	0.791 ± 0.014
Radial velocity semi-amplitude variation K (m s^{-1})	$\mathcal{U}[0, 50]$	10.6 ± 3.0
GP period P_{GP} (d)	$\mathcal{U}[4, 5.1]$	4.315 ± 0.014
λ_P	$\mathcal{U}[0.1, 2]$	$0.558^{+0.082}_{-0.069}$
λ_e	$\mathcal{U}[1, 300]$	$31.2^{+7.6}_{-6.3}$
V_c (km s^{-1})	$\mathcal{U}[0, 0.1]$	$0.0058^{+0.0049}_{-0.0037}$
V_r (km s^{-1})	$\mathcal{U}[-1, 1]$	$0.0421^{+0.0147}_{-0.0095}$
L_c	$\mathcal{U}[0, 1]$	$0.0242^{+0.0079}_{-0.0055}$
B_c (km s^{-1})	$\mathcal{U}[-1.5, 1.5]$	$0.020^{+0.061}_{-0.059}$
B_r (km s^{-1})	$\mathcal{U}[-0.5, 0.5]$	$-0.086^{+0.037}_{-0.049}$
Offset HARPS-N (km s^{-1})	$\mathcal{U}[34.1998, 34.5825]$	34.393 ± 0.003
Offset log R'_{HK}	$\mathcal{U}[-4.5878, -4.2885]$	-4.45 ± 0.01
Offset BIS (km s^{-1})	$\mathcal{U}[-1.5568, 0.6372]$	-0.04 ± 0.04
Jitter term $\sigma_{HARPS-N}$ (m s^{-1})	$\mathcal{U}[0, 100]$	$2.60^{+3.15}_{-2.05}$
Jitter term $\sigma_{\log R'_{HK}}$	$\mathcal{U}[0, 1]$	$0.003\,0 \pm 0.002\,1$
Jitter term BIS (m s^{-1})	$\mathcal{U}[0, 1000]$	291^{+27}_{-24}
Limb darkening q_1 for *K2* C5	$\mathcal{U}[0, 1]$	$0.27^{+0.08}_{-0.07}$
Limb darkening q_2 for *K2* C5	$\mathcal{U}[0, 1]$	$0.13^{+0.19}_{-0.10}$
Limb darkening q_1 for *K2* C18	$\mathcal{U}[0, 1]$	$0.27^{+0.08}_{-0.07}$
Limb darkening q_2 for *K2* C18	$\mathcal{U}[0, 1]$	$0.13^{+0.19}_{-0.10}$
Limb darkening q_1 for ARCTIC	$\mathcal{U}[0, 1]$	$0.03^{+0.06}_{-0.02}$
Limb darkening q_2 for ARCTIC	$\mathcal{U}[0, 1]$	$0.40^{+0.36}_{-0.28}$
Limb darkening q_1 for MUSCAT2 r'	$\mathcal{U}[0, 1]$	$0.73^{+0.19}_{-0.26}$
Limb darkening q_2 for for MUSCAT2 r'	$\mathcal{U}[0, 1]$	$0.49^{+0.13}_{-0.15}$
Limb darkening q_1 for MUSCAT2 i'	$\mathcal{U}[0, 1]$	$0.57^{+0.27}_{-0.26}$
Limb darkening q_2 for MUSCAT2 i'	$\mathcal{U}[0, 1]$	$0.47^{+0.22}_{-0.23}$
Limb darkening q_1 for MUSCAT2 z'	$\mathcal{U}[0, 1]$	$0.73^{+0.19}_{-0.26}$
Limb darkening q_2 for MUSCAT2 z'	$\mathcal{U}[0, 1]$	$0.47^{+0.22}_{-0.23}$
Jitter term σ_{K2C5} ($\times 10^{-6}$)	$\mathcal{U}[0, 1 \times 10^3]$	40 ± 4
Jitter term σ_{K2C18} ($\times 10^{-6}$)	$\mathcal{U}[0, 1 \times 10^3]$	52 ± 4
Jitter term σ_{ARCTIC} ($\times 10^{-6}$)	$\mathcal{U}[0, 1 \times 10^3]$	267 ± 50
Jitter term $\sigma_{MUSCAT2r'}$ ($\times 10^{-6}$)	$\mathcal{U}[0, 1 \times 10^5]$	1321 ± 27
Jitter term $\sigma_{MUSCAT2i'}$ ($\times 10^{-6}$)	$\mathcal{U}[0, 1 \times 10^5]$	1419 ± 30
Jitter term $\sigma_{MUSCAT2z'}$ ($\times 10^{-6}$)	$\mathcal{U}[0, 1 \times 10^5]$	1919 ± 38
Derived parameters		
Planet mass (M$_\oplus$)	–	21.8 ± 6.2
Planet radius (R$_\oplus$)	–	3.88 ± 0.16
Planet density (g cm^{-3})	–	$2.04^{+0.66}_{-0.61}$
Semi-major axis a (au)	–	$0.0301 \pm 0.001\,4$
Orbital inclination i (deg)	–	81.27 ± 0.37
Equilibrium temperature[c] T_{eq} (K)	–	$1\,841 \pm 41$
Insolation F_p (F$_\oplus$)	–	1915^{+178}_{-165}
Planet surface gravity[d] (cm s^{-2})	–	1536^{+436}_{-442}
Planet surface gravity (cm s^{-2})	–	1421^{+427}_{-413}

Note. – [a] $\mathcal{U}[a, b]$ refers to uniform priors between a and b, $\mathcal{N}[a, b]$ to Gaussian priors with median a and standard deviation b, and $\mathcal{F}[a]$ to a fixed value a. [b] Inferred parameters and errors are defined as the median and 68.3% credible interval of the posterior distribution. [c] Assuming albedo = 0. [d] Calculated from the scaled-parameters as in Southworth, Wheatley & Sams (2007).
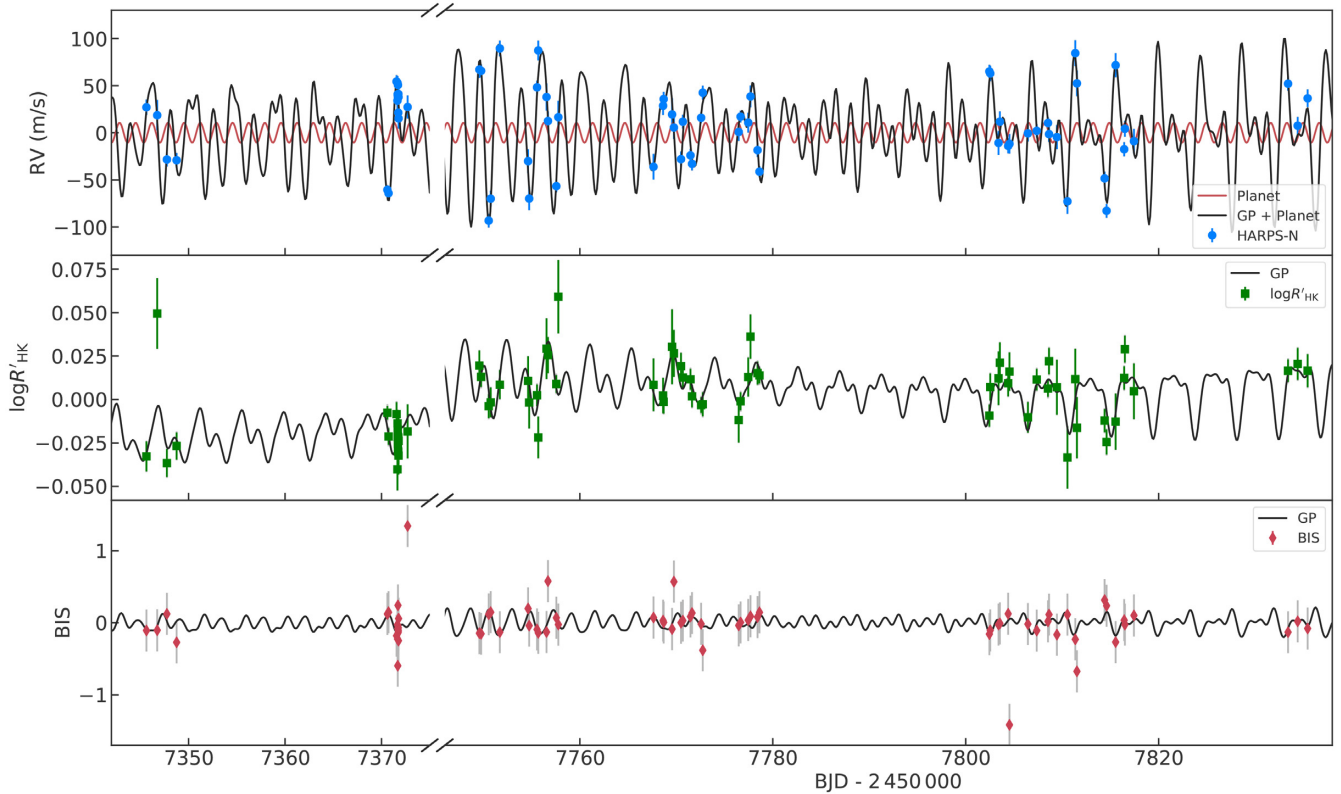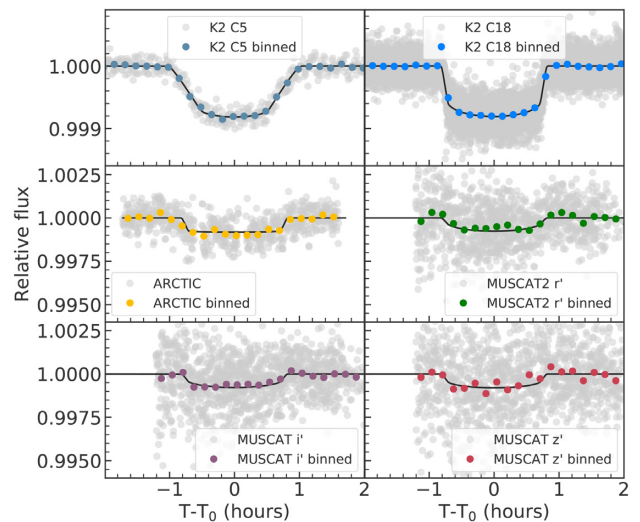
Figure 2. Radial velocity (top), log $R'_{\rm HK}$ (middle) and BIS (bottom) time series. All time series have been corrected by the inferred offset. Inferred models are presented as solid continuous lines. Measurements are shown with filled symbols with error bars. Gray error bars account for the jitter. We note that there is a gap between 7375 and 7746 BJD - 2450000 where there were no measurements.
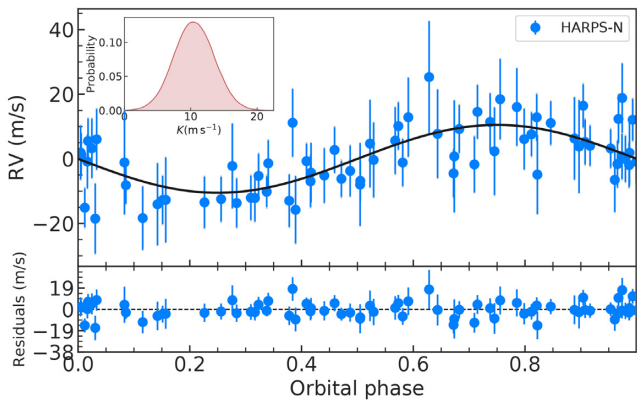

Figure 3. RV curve of K2-100 folded to the orbital period of K2-100b. HARPS-N data (blue circles) are shown following the subtraction of the instrumental offset and GP model. Gray error bars account for the jitter. The Keplerian solution is shown as a solid line. Top-left inset displays the posterior distribution for K.

Figure 4. K2-100b transits. Each panel shows a flattened light curve from different instruments folded to the orbital period of K2-100b. Black lines show the best-fitting transit models.

Hillenbrand (2008), modified to match the present-day rotation period, but with a free parameter x allowing us to vary the spin-down rate prior to 2 Gyr (see K19, for details). The instantaneous high-energy X-ray + EUV (XUV) emission of the host star is estimated from the rotation period following Wright et al. (2011), allowing us to explore a wide range of scenarios for the integrated XUV budget of the planet over its lifetime.

As described in K19, we apply a Monte Carlo approach to fit the observed planetary radius, using the other system parameters and their uncertainties as inputs, finally obtaining probability distribution functions for x and the initial atmospheric mass fraction (i.e. ratio between atmospheric mass and planetary mass at an age
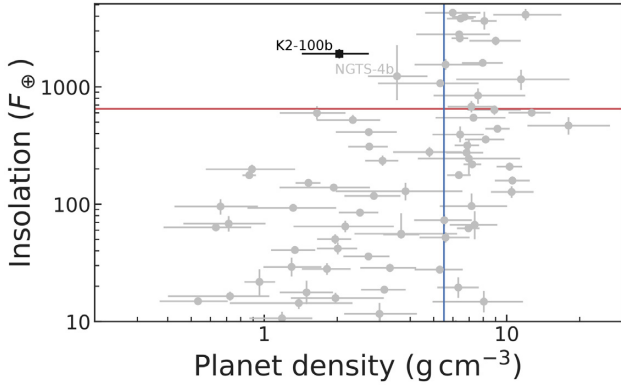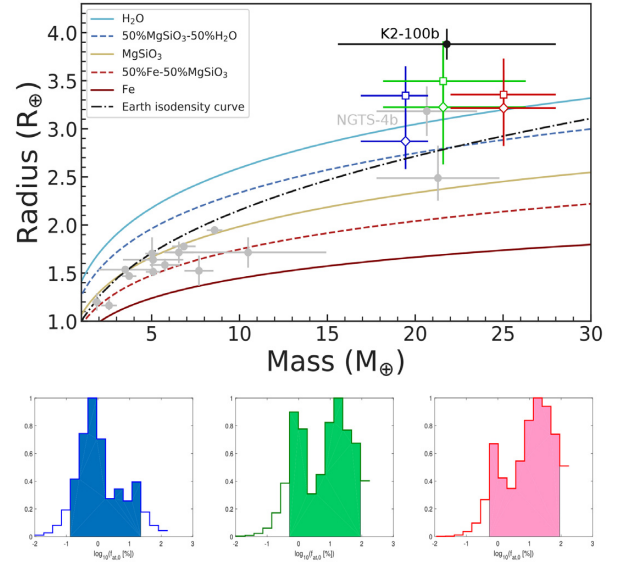
Figure 5. Planet density versus insolation for small ($R_p < 4\,R_\oplus$) transiting planets (gray circles). The location of K2-100b is marked with a black square. We also label NGTS-4b. Horizontal red line shows the insolation limit of 650 $F_\oplus$ given by Lundkvist et al. (2016). Vertical blue line corresponds to Earth's density.

Figure 6. Top: Mass versus radius diagram for small ($R_p < 4\,R_\oplus$) planets which receive an insolation >650 larger than the Earth (gray circles). The location of K2-100b is marked with a black circle. Its predicted planetary mass and radius at 2 and 5 Gyr is shown with empty squares and diamonds, respectively, with colours corresponding to different initial rotation rates XUV fluxes for the star: fast/high (red), moderate (green) and slow/low (blue) (see the text for details). Zeng et al. (2016)'s composition models are displayed with different colour lines. Bottom: Posterior distributions obtained for the initial atmospheric mass fraction $f_{at,0}$ assuming the three different regimes of evolution of the stellar XUV flux. The shaded areas correspond to the 68 per cent region of the credible interval of the posterior distribution.

of 5 Myr; $f_{at,0}$) as output. Altogether, the input parameters of the Monte Carlo simulation are planetary mass, orbital separation, age of the system, stellar mass, and present-day rotation period.[1] We then use the results to evolve the planetary atmosphere beyond its current age and up to 5 Gyr, computing the planetary radius and f_{at} as a function of age and for three different ranges of x corresponding to rotation rates at an age of 150 Myr of less than 0.5 d, between 0.5 and 3 d, and more than 3 d. At an age of 150 Myr, these rotation rates translate to XUV fluxes in the range 376–600, 117–376, and 13–117 times larger than the current solar XUV emission, respectively. Throughout, we assume a core density equal to Earth's bulk density, which sets the core radius.

Fig. 6 shows the current position of the planet in the mass–radius diagram and those predicted to be possible at 2 and 5 Gyr, for the three different ranges of x we considered. Our results indicate that after 5 Gyrs the planet is likely to lose a significant amount of its primordial hydrogen-dominated atmosphere, finally retaining between about 0.1 and 0.7 per cent of its mass in the atmosphere, depending on the evolutionary path of the stellar XUV emission and on planetary mass. In particular, for a planetary mass below about 20 $M_\oplus$ it is unlikely that the planet will retain more than 0.1 per cent of its mass in the atmosphere and therefore its predicted radius at 5 Gyr is close to the assumed core radius. In some cases, when considering planetary masses below 18 $M_\oplus$, we reach the (almost) complete escape of the primary atmosphere before 2 Gyr.

In case the actual planetary mass is above about 20 $M_\oplus$, the planet could still keep up to 0.7 per cent of its mass in the atmosphere, as shown in Fig. 6. This plot shows that if K2-100 evolves as described by our fast rotator model, K2-100b should have a relatively high core mass, which is able to retain a significant volatile envelope. This could be similar to the case of NGTS-4b. On the other extreme, if K2-100 evolves as a slow rotator, which is possible if the planet has a mass closer to the lower mass limit given by the RV measurements,

K2-100b would end up as a core with an Earth-like density, similar to the other highly irradiated planets.

As shown by K19, and illustrated on Fig. 6, for a given stellar evolution scenario, the observed present-day radius of the planet can only be matched for a certain range of masses, which is within the mass range allowed (at the 1σ level) by our RV results. We were unable to fit the observed present-day radius with any atmospheric evolution scenario for planet masses below 15 $M_\oplus$: at such low planetary masses, the atmosphere essentially escapes entirely before the age of Praesepe, even if we assume that the initial stellar XUV flux was rather low.

Fig. 6 also presents the posterior distributions we obtained for the initial planetary atmospheric mass fraction $f_{at,0}$ for the three different ranges of x we considered. Larger XUV fluxes imply that more atmosphere has already escaped, so that the initial atmospheric mass fraction must have been larger (though the range of allowed values is also larger). Our results indicate that the planet may be subject to substantial atmospheric escape throughout most of its lifetime with the strongest escape happening during the first few hundred Myrs. In particular, for masses larger than about 20 $M_\oplus$ atmospheric escape remains significant for Gyrs, implying that the planetary radius will keep decreasing, hence evolving, also after the first few hundred Myrs during which the planetary radius can decrease dramatically.

In all of the models that fit the available data, the planet is currently hosting an escaping atmosphere: using the code described by K18b, we computed a series of hydrodynamic models of the planetary upper atmosphere for the range of planet parameters spanned

---

[1]The planetary equilibrium temperature, which is one of the input parameters for extracting the mass-loss rates (by setting the lower boundary of the hydrodynamic modelling) and atmospheric mass fractions from the grids, is set by the orbital separation and stellar parameters, where the latter are derived from the MESA evolutionary tracks and the stellar mass.

by the evolution models that fit the observational constraints. These yield present-day atmospheric mass-loss rates in the range 10^{11}–10^{12} g s^{-1}.

5 CONCLUSIONS

We showed how, by combining RV with activity indicators, we can disentangle planetary and activity RV variations for young active stars. These results encourage the RV follow-up of young or active stars to be discovered with missions such as *TESS* and *PLATO*.

We measured a mass of 21.8 ± 6.2 M$_\oplus$ for K2-100b, a 3.88 ± 0.16 R$_\oplus$ planet transiting a star in the Praesepe cluster. We estimated that the relative high irradiation received by the planet implies that its atmosphere is currently evaporating. This makes K2-100 an excellent laboratory to test photoevaporation models.

REFERENCES

Adams F. C., Laughlin G., 2006, ApJ, 649, 1004
Aigrain S., Pont F., Zucker S., 2012, MNRAS, 419, 3147
Barragán O., Gandolfi D., 2017, Astrophysics Source Code Library, record ascl:1706.001
Barragán O. et al., 2018a, MNRAS, 475, 1765
Barragán O. et al., 2018b, A&A, 612, A95
Barragán O., Gandolfi D., Antoniciello G., 2019, MNRAS, 482, 1017
Boesgaard A. M., Roper B. W., Lum M. G., 2013, ApJ, 775, 58
Bossini D. et al., 2019, A&A, 623, A108
Brandt T. D., Huang C. X., 2015, ApJ, 807, 24
Bressan A., Marigo P., Girardi L., Salasnich B., Dal Cero C., Rubele S., Nanni A., 2012, MNRAS, 427, 127
Bruntt H. et al., 2010, MNRAS, 405, 1907
Burnham K., Anderson D., 2002, Model Selection and Multimodel Inference: A Practical Information-Theoretic Approach. Springer-Verlag, New York
Choi J., Dotter A., Conroy C., Cantiello M., Paxton B., Johnson B. D., 2016, ApJ, 823, 102
David T. J. et al., 2016a, AJ, 151, 112
David T. J. et al., 2016b, Nature, 534, 658
David T. J. et al., 2019, AJ, 158, 79
Doyle A. P., Davies G. R., Smalley B., Chaplin W. J., Elsworth Y., 2014, MNRAS, 444, 3592
Fridlund M. et al., 2017, A&A, 604, A16
Gaia Collaboration et al., 2018, A&A, 616, A1
Gandolfi D. et al., 2008, ApJ, 687, 1303
Gandolfi D. et al., 2017, AJ, 154, 123
Grunblatt S. K., Howard A. W., Haywood R. D., 2015, ApJ, 808, 127
Haywood R. D. et al., 2014, MNRAS, 443, 2517
Howell S. B. et al., 2014, PASP, 126, 398
Jackson B., Greenberg R., Barnes R., 2008, ApJ, 678, 1396
Johnstone C. P. et al., 2015, ApJ, 815, L12
Kipping D. M., 2010, MNRAS, 408, 1758
Kipping D. M., 2013, MNRAS, 435, 2152
Kraus A. L., Hillenbrand L. A., 2007, AJ, 134, 2340
Kubyshkina D., Lendl M., Fossati L., Cubillos P. E., Lammer H., Erkaev N. V., Johnstone C. P., 2018a, A&A, 612, A25
Kubyshkina D. et al., 2018b, A&A, 619, A151
Kubyshkina D. et al., 2019, ApJ, 879, 26
Kurucz R. L., 2013, Astrophysics Source Code Library, record ascl:1303.024
Libralato M. et al., 2016, MNRAS, 463, 1780
Lightkurve Collaboration et al., 2018, Astrophysics Source Code Library, record ascl:1812.013
Livingston J. H. et al., 2018a, AJ, 155, 115
Livingston J. H. et al., 2018b, AJ, 156, 277
Livingston J. H. et al., 2019, MNRAS, 484, 8
Lundkvist M. S. et al., 2016, Nature Commun., 7, 11201
Malavolta L. et al., 2018, AJ, 155, 107
Mamajek E. E., Hillenbrand L. A., 2008, ApJ, 687, 1264
Mann A. W. et al., 2016a, AJ, 152, 61
Mann A. W. et al., 2016b, ApJ, 818, 46
Mann A. W. et al., 2017, AJ, 153, 64
Mann A. W. et al., 2018, AJ, 155, 4
Mermilliod J. C., 1987, A&AS, 71, 413
Morton T. D., 2012, ApJ, 761, 6
Narita N. et al., 2019, J. Astron. Telescopes Instrum. Syst., 5, 015001
Owen J. E., Wu Y., 2013, ApJ, 775, 105
Pace G., Pasquini L., François P., 2008, A&A, 489, 403
Parviainen H., 2015, MNRAS, 450, 3233
Parviainen H., Aigrain S., 2015, MNRAS, 453, 3822
Parviainen H. et al., 2019, preprint (arXiv:1907.09776)
Pecaut M. J., Mamajek E. E., 2013, ApJS, 208, 9
Pepe F. et al., 2013, Nature, 503, 377
Pepper J. et al., 2017, AJ, 153, 177
Persson C. M. et al., 2018, A&A, 618, A33
Petigura E. A. et al., 2015, ApJ, 811, 102
Piskunov N., Valenti J. A., 2017, A&A, 597, A16
Pope B. J. S., Parviainen H., Aigrain S., 2016, MNRAS, 461, 3399
Rajpaul V., Aigrain S., Osborne M. A., Reece S., Roberts S., 2015, MNRAS, 452, 2269
Rajpaul V., Aigrain S., Roberts S., 2016, MNRAS, 456, L6
Raymond S. N., Barnes R., Veras D., Armitage P. J., Gorelick N., Greenberg R., 2009, ApJ, 696, L98
Ryabchikova T., Piskunov N., Kurucz R. L., Stempels H. C., Heiter U., Pakhomov Y., Barklem P. S., 2015, Phys. Scr., 90, 054005

Salaris M., Weiss A., Percival S. M., 2004, A&A, 414, 163
Southworth J., 2011, MNRAS, 417, 2166
Southworth J., Wheatley P. J., Sams G., 2007, MNRAS, 379, L11
Stefansson G., Li Y., Mahadevan S., Wisniewski J., Hebb L., Morris B., Huehnerhoff J., Hawley S., 2018, AJ, 156, 266
Valenti J. A., Piskunov N., 1996, A&AS, 118, 595
van Leeuwen F., 2009, A&A, 497, 209
Vanderburg A., Johnson J. A., 2014, PASP, 126, 948

West R. G. et al., 2019, MNRAS, 486, 5094
Winn J. N., 2010, preprint (arXiv:1001.2010)
Wright N. J., Drake J. J., Mamajek E. E., Henry G. W., 2011, ApJ, 743, 48
Yee S. W., Petigura E. A., von Braun K., 2017, ApJ, 836, 77
Zeng L., Sasselov D. D., Jacobsen S. B., 2016, ApJ, 819, 127

APPENDIX: HARPS-N MEASUREMENTS

Table A1. Radial velocity, activity, and symmetry indicators measurements for K2-100.

Time (BJD$_{TDB}$-2450000)	RV (km s^{-1})	σ_{RV} (km s^{-1})	CCF BIS (km s^{-1})	CCF FWHM (km s^{-1})	Log R'_{HK}	$\sigma_{\log R'_{HK}}$	S/N
7345.63288	34.4200	0.0080	21.1143	−0.1473	−4.4804	0.0086	51.3
7346.74932	34.4116	0.0161	20.8156	−0.1438	−4.3982	0.0203	28.1
7347.75251	34.3646	0.0074	20.8381	0.0827	−4.4842	0.0080	54.2
7348.75941	34.3638	0.0076	20.9736	−0.3119	−4.4744	0.0078	54.2
7351.70898	34.0950	0.0453	21.1253	0.6314	−4.3827	0.0741	11.3
7351.73144	33.6321	0.1215	24.0350	1.0506	−3.9538	0.1979	2.3
7352.72840	34.1035	0.0536	21.8887	0.4047	−4.4255	0.1046	9.1
7352.74247	33.7331	0.0485	23.0619	2.5142	−4.2920	0.0653	10.4
7370.61016	34.3325	0.0048	20.7341	0.0814	−4.4553	0.0039	82.2
7370.72940	34.3289	0.0054	20.7907	0.1057	−4.4689	0.0048	70.9
7371.55846	34.4474	0.0067	20.7710	−0.2209	−4.4561	0.0069	60.1
7371.65315	34.4271	0.0100	20.8869	−0.0685	−4.4878	0.0121	42.4
7371.66420	34.4457	0.0075	20.8768	−0.2659	−4.4614	0.0075	53.3
7371.67486	34.4338	0.0070	20.9119	−0.1224	−4.4692	0.0069	56.4
7371.68506	34.4326	0.0071	20.8996	−0.6367	−4.4650	0.0070	55.3
7371.69614	34.4302	0.0069	21.0014	−0.0799	−4.4731	0.0067	57.4
7371.70673	34.4437	0.0064	20.9632	0.2011	−4.4688	0.0060	60.7
7371.71745	34.4300	0.0065	20.9909	−0.1295	−4.4773	0.0062	60.6
7371.72832	34.4315	0.0065	20.9366	−0.1761	−4.4703	0.0064	59.7
7371.73898	34.4143	0.0060	20.9340	−0.1083	−4.4778	0.0056	64.6
7371.74885	34.4342	0.0069	21.0073	−0.1534	−4.4696	0.0068	57.3
7371.76023	34.4309	0.0092	21.0583	−0.2884	−4.4799	0.0108	44.6
7371.77033	34.4082	0.0108	21.0351	0.0180	−4.4715	0.0135	38.6
7372.67782	34.2780	0.0548	20.2459	−0.0747	−4.3204	0.0816	9.3
7372.70837	34.4203	0.0122	20.6497	1.3029	−4.4660	0.0155	35.1
7749.58185	34.4601	0.0088	18.9395	−0.1852	−4.4281	0.0086	44.7
7749.76345	34.4587	0.0067	18.9701	−0.1929	−4.4346	0.0058	59.4
7750.55088	34.2998	0.0072	18.9979	0.0767	−4.4515	0.0069	57.0
7750.75882	34.3231	0.0084	18.8521	0.1063	−4.4493	0.0085	49.7
7751.70251	34.4825	0.0083	18.9755	−0.1709	−4.4391	0.0083	49.8
7754.63363	34.3629	0.0124	21.0214	0.1569	−4.4369	0.0141	32.8
7754.74514	34.3232	0.0122	20.9659	−0.0801	−4.4494	0.0148	34.6
7755.56052	34.4412	0.0068	20.3272	−0.1334	−4.4452	0.0062	58.3
7755.68564	34.4804	0.0105	20.6427	−0.1800	−4.4695	0.0119	40.5
7756.54391	34.4309	0.0144	20.9620	−0.1692	−4.4184	0.0174	31.2
7756.69497	34.4055	0.0100	21.1398	0.5372	−4.4221	0.0103	42.5
7757.56227	34.3364	0.0062	20.5935	0.0287	−4.4387	0.0051	64.3
7757.76849	34.4096	0.0173	20.5733	−0.0650	−4.3885	0.0211	26.6
7767.63488	34.3569	0.0135	20.6536	0.0321	−4.4392	0.0151	32.2
7768.62766	34.4216	0.0098	20.7994	−0.0101	−4.4454	0.0101	40.1
7768.68724	34.4287	0.0074	20.8263	−0.0352	−4.4490	0.0067	55.8
7769.56123	34.4124	0.0173	20.8606	−0.1276	−4.4173	0.0215	26.8
7769.74871	34.3985	0.0120	20.9550	0.5301	−4.4211	0.0134	36.7

Table A1 – *continued*

Time (BJD$_{\rm TDB}$-2450000)	RV (km s^{-1})	$\sigma_{\rm RV}$ (km s^{-1})	CCF BIS (km s^{-1})	CCF FWHM (km s^{-1})	Log $R'_{\rm HK}$	$\sigma_{\log R'_{\rm HK}}$	S/N
7770.48664	34.3650	0.0080	20.7612	− 0.0388	−4.4285	0.0076	51.3
7770.67781	34.4047	0.0071	20.6799	− 0.0105	−4.4350	0.0065	56.8
7771.46646	34.3690	0.0067	21.0110	0.0454	−4.4360	0.0060	60.7
7771.62722	34.3601	0.0070	20.7487	0.0950	−4.4458	0.0063	57.5
7772.57081	34.4089	0.0055	20.5872	− 0.0564	−4.4509	0.0045	71.3
7772.74143	34.4355	0.0073	20.5553	− 0.4219	−4.4504	0.0069	57.2
7776.46636	34.3938	0.0094	20.8932	− 0.0770	−4.4595	0.0129	47.7
7776.66380	34.4101	0.0062	20.7195	− 0.0348	−4.4487	0.0052	65.2
7777.45522	34.4037	0.0104	20.8038	− 0.0037	−4.4347	0.0112	41.2
7777.68914	34.4315	0.0116	20.5416	0.0484	−4.4115	0.0127	37.6
7778.41974	34.3745	0.0072	20.9883	0.0391	−4.4324	0.0066	57.8
7778.62073	34.3518	0.0057	20.7787	0.1042	−4.4338	0.0046	69.2
7802.45286	34.4581	0.0068	20.4947	− 0.1972	−4.4569	0.0063	58.7
7802.54483	34.4560	0.0081	20.6486	− 0.1455	−4.4405	0.0078	50.5
7803.39940	34.3822	0.0127	20.6459	− 0.0650	−4.4355	0.0154	34.5
7803.54249	34.4048	0.0107	20.4169	− 0.0496	−4.4265	0.0117	39.2
7804.40126	34.3790	0.0078	20.8478	0.0843	−4.4383	0.0075	52.5
7804.53623	34.3812	0.0103	20.6631	− 1.4568	−4.4316	0.0110	40.8
7806.44739	34.3924	0.0087	20.5212	− 0.0588	−4.4579	0.0088	47.8
7807.36241	34.3950	0.0069	21.3158	− 0.1485	−4.4362	0.0062	59.0
7808.52958	34.4034	0.0059	21.0225	− 0.0204	−4.4413	0.0048	68.2
7808.63565	34.3915	0.0082	20.9503	0.0738	−4.4256	0.0076	51.6
7809.45282	34.3884	0.0128	20.7297	− 0.2052	−4.4406	0.0158	34.2
7810.54426	34.3202	0.0132	20.3217	0.0739	−4.4810	0.0179	33.4
7811.35884	34.4775	0.0137	20.7007	− 0.2704	−4.4359	0.0174	32.9
7811.52928	34.4454	0.0136	21.1617	− 0.7146	−4.4639	0.0176	31.8
7814.39794	34.3446	0.0070	21.1399	0.2747	−4.4598	0.0066	57.5
7814.60206	34.3102	0.0073	20.8498	0.1962	−4.4721	0.0072	57.4
7815.54132	34.4647	0.0127	20.7258	− 0.3086	−4.4604	0.0161	34.7
7816.42836	34.3755	0.0074	20.5119	− 0.0049	−4.4353	0.0067	54.8
7816.49993	34.3972	0.0083	20.5529	− 0.0658	−4.4187	0.0077	50.1
7817.43947	34.3840	0.0131	21.0605	0.0611	−4.4429	0.0160	33.9
7833.41663	34.4450	0.0072	21.0347	− 0.1712	−4.4311	0.0065	56.5
7834.41427	34.4005	0.0091	21.2186	− 0.0202	−4.4272	0.0092	44.9
7835.44577	34.4296	0.0094	20.8092	− 0.1197	−4.4311	0.0095	43.6

[1] *Sub-department of Astrophysics, Department of Physics, University of Oxford, Oxford, OX1 3RH, UK*

[2] *Space Research Institute, Austrian Academy of Sciences, Schmiedlstrasse 6, A-8041 Graz, Austria*

[3] *Dipartimento di Fisica, Università di Torino, via P. Giuria 1, I-10125 Torino, Italy*

[4] *Department of Astronomy, University of Tokyo, 7-3-1 Hongo, Bunkyo-ku, Tokyo 113-0033, Japan*

[5] *Department of Earth and Space Sciences, Chalmers University of Technology, Onsala Space Observatory, SE-439 92 Onsala, Sweden*

[6] *Leiden Observatory, University of Leiden, PO Box 9513, NL-2300 RA, Leiden, the Netherlands*

[7] *Rheinisches Institut für Umweltforschung an der Universität zu Köln, Aachener Strasse 209, D-50931 Köln, Germany*

[8] *Instituto de Astrofísica de Canarias, E-38205 La Laguna, Tenerife, Spain*

[9] *Departamento de Astrofísica, Universidad de La Laguna, E-38206 La Laguna, Tenerife, Spain*

[10] *INAF - Osservatorio Astrofisico di Catania, Via S. Sofia 78, I-95123 Catania, Italy*

[11] *Astrophysics Group, Cavendish Laboratory, University of Cambridge, J. J. Thomson Avenue, Cambridge CB3 0HE, UK*

[12] *Dipartimento di Fisica e Astronomia 'Galileo Galilei', Università di Padova, Vicolo dell'Osservatorio 3, I-35122, Padova, Italy*

[13] *Astrobiology Center, 2-21-1 Osawa, Mitaka, Tokyo 181-8588, Japan*

[14] *JST, PRESTO, 2-21-1 Osawa, Mitaka, Tokyo 181-8588, Japan*

[15] *National Astronomical Observatory of Japan, 2-21-1 Osawa, Mitaka, Tokyo 181-8588, Japan*

[16] *Stellar Astrophysics Centre, Department of Physics and Astronomy, Aarhus University, Ny Munkegade 120, DK-8000 Aarhus C, Denmark*

[17] *INAF - Osservatorio Astronomico di Padova, Vicolo dell'Osservatorio 5, Padova, I-3512, Italy*

[18] *Institute of Planetary Research, German Aerospace Center, Rutherford-strasse 2, D-12489 Berlin, Germany*

[19] *Department of Astronomy and McDonald Observatory, University of Texas at Austin, 2515 Speedway, Stop C1400, Austin, TX 78712, USA*

[20] *Department of Earth and Planetary Science, The University of Tokyo, 7-3-1Hongo, Bunkyo-ku, Tokyo 113-0033, Japan*
[21] *Thüringer Landessternwarte Tautenburg, Sternwarte 5, D-07778 Tautenburg, Germany*
[22] *Center for Astrophysics, Harvard & Smithsonian, 60 Garden Street, Cambridge, MA 02138, USA*

[23] *Space Telescope Science Institute, 3700 San Martin Drive, Baltimore, MD 21218, USA*
[24] *Astronomy Department and Van Vleck Observatory, Wesleyan University, Middletown, CT 06459, USA*

This paper has been typeset from a TEX/LATEX file prepared by the author.